Journal of Power Sources 594 (2024) 233948

Contents lists available at ScienceDirect

Journal of Power Sources

journal homepage: www.elsevier.com/locate/jpowsour

Temperature-driven path dependence in Li-ion battery cyclic aging

Max Feinauer [a], Margret Wohlfahrt-Mehrens [a,b], Markus Hölzle [a], Thomas Waldmann [a,b,*]

[a] Zentrum für Sonnenenergie- und Wasserstoff-Forschung Baden-Württemberg (ZSW), Lise-Meitner-Straße 24, 89081, Ulm, Germany
[b] Helmholtz Institute Ulm for Electrochemical Energy Storage (HIU), Helmholtzstraße 11, 89081, Ulm, Germany

HIGHLIGHTS

- Aging color maps illustrate changing aging rate.
- Cyclic aging at elevated temperatures is little affected by previous aging.
- Low temperature cycling with Li plating accelerates further Li plating.
- Aging at high temperatures shifts onset of Li plating to lower temperatures.
- Permutability of aging temperatures is analyzed by means of commutators.

GRAPHICAL ABSTRACT

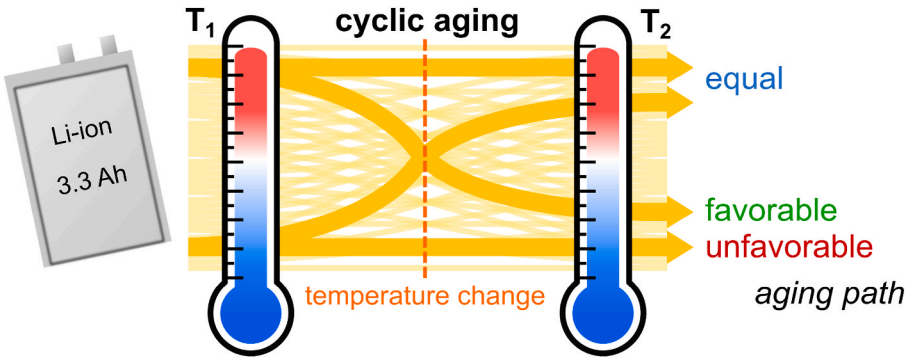

ARTICLE INFO

Keywords:
Li-ion batteries
Aging mechanisms
Temperature variation
Path dependence
Arrhenius plots
Li plating

ABSTRACT

Operation temperature is known to be one of the most impacting parameters for aging of Li-ion batteries under cycling conditions. While Li plating usually dominates aging at low temperatures, Solid-Electrolyte-Interphase (SEI) growth often dominates aging at elevated temperatures. The longest cycle life for Li-ion batteries is observed at the crossover temperature of both aging mechanisms at around 25 °C. We introduce aging color maps to show changes in the aging rate during battery aging. Reconstructed 3-electrode full cells with Li reference electrode show that the prolonged CV phase during charging at low temperatures counteracts Li plating by an increasing anode potential. Thirty-six temperature variations during cycling between 0 °C and 45 °C were studied to investigate the temperature path dependence of battery aging. The permutability of aging temperatures is analyzed by means of commutators. It turns out that aging at elevated temperatures is only slightly affected by previous aging processes and aging at lower temperatures with Li plating accelerates itself. Previous high temperature cycling decelerates Li plating and shifts its onset to lower temperatures, leading to a new and improved optimum cycling temperature of 20 °C. Differential voltage analysis and Post-Mortem analysis were performed to identify the underlying aging mechanisms.

* Corresponding author. ZSW – Zentrum für Sonnenenergie- und Wasserstoff-Forschung Baden-Württemberg, Helmholtzstraße 8, D-89081, Ulm, Germany.
E-mail address: thomas.waldmann@zsw-bw.de (T. Waldmann).

https://doi.org/10.1016/j.jpowsour.2023.233948
Received 21 September 2023; Received in revised form 9 November 2023; Accepted 8 December 2023
Available online 7 January 2024

Journal of power sources

Special Issue: Lithium Battery Degradation & Aging: Experimental Characterization, Monitoring and Modelling.

1. Introduction

Li-ion batteries have become an indispensable part of our daily lives and are by far the most widely used electrochemical energy storage system, with ongoing demand growth [1]. High and continuously improving energy and power densities, high efficiencies and constantly decreasing prices contribute to the success of Li-ion batteries in a wide range of applications [2]. Even though lifetimes of Li-ion batteries have reached an acceptable level, there is still potential for further improvement. It is understood that aging conditions strongly influence battery cycle life, i.e. power and energy loss [3–8]. Aging conditions during storage or operation lead to a number of different aging mechanisms including cathode, anode, and electrolyte decomposition, interfacial layer growth, or Li plating [7,9–11]. The complexity of aging is compounded by additional variables such as the choice of electrode and electrolyte materials, cell geometry, or even electrode processing [8]. In general, cyclic aging is complex to understand due to an overlap with calendar aging processes, whereby mild aging conditions lead to larger contributions of calendar aging [12–15].

In addition to charge- and discharge rate and cycling voltage range, temperature is one of the most influential operating conditions [8, 15–19]. The wide range of applications of Li-ion batteries leads to an equally wide range of operating and storage temperatures. While larger-size applications such as batteries in electric vehicles allow active temperature control systems, smaller applications such as e-scooters or power tools do not have an active temperature control and as a consequence a highly variable temperature.

The temperature dependence of a chemical reaction rate can be described by the Arrhenius law [4,20]. The rate constant r is given by

$$r = A \cdot \exp\left(-\frac{E_a}{k_B T} \right) \tag{1}$$

with T as the absolute temperature and k_B as the Boltzmann constant. The Arrhenius parameters, i.e., the pre-exponential factor A and the apparent activation energy E_a, are typically determined by plotting $\ln(r)$ versus $1/k_B T$ in a so-called Arrhenius plot.

Arrhenius plots of the aging rate of batteries, in particular for storage, are known for a long time [3–6,21,22]. The rate constant corresponds thereby to the aging rate of the battery, i.e. the capacity loss per time or cycle.

In 2014, our group has applied the Arrhenius law for the first time to the cyclic aging process of Li-ion batteries covering the full operational temperature window [4]. The Arrhenius plot for the cyclic aging rate consists of two branches arranged in a V-shape with a crossing around 25 °C. This indicates two different aging mechanisms, namely Solid-Electrolyte-Interface (SEI) growth in the high temperature range and Li plating in the low temperature range [4,6,21,23].

The SEI composes of mostly Li containing electrolyte decomposition products and is initially formed during formation by side reactions at the anode-electrolyte interface [24]. It further growths with time and cycling [13,24,25]. The exact SEI composition and morphology is unique to each anode material, electrolyte (solvent, salt, and additives), and formation condition, and thereby affects capacity loss through continuous Li consumption [24]. An Arrhenius law can describe the increasing SEI growth rate with temperature and explains the accelerated capacity loss at higher temperatures [26,27]. The capacity degradation due to loss of Li inventory (LLI) during calendar aging can be described by a square root of time dependence, as typically done for diffusion limited layer growth [27,28]. In contrast, cyclic aging behavior is influenced by additional factors and its aging rate is beyond what is captured by calendar aging [17,29]. Heidrich et al. showed that the SEI thickness is limited, although an increased SEI dissolution occurs at elevated temperatures, coupled with a subsequent re-forming and Li consumption [30]. In addition, Wu et al. claim a stabilization of the SEI at higher temperatures [8].

While battery storage at low temperatures results in low SEI growth rates, Li plating becomes the dominant aging mechanism during charging. Li plating occurs instead of chemical intercalation into the anode at negative anode potentials vs. Li/Li^+ during charging. It is caused by poor electrode kinetics at high currents, especially at low temperatures [21,31]. The anode diffusion coefficient increases with temperature, following an Arrhenius law [32,33]. Furthermore, there is an Arrhenius dependence of the exchange current between oxidation and reduction of Li, affecting directly the overpotential [32,34,35]. Since lower anode diffusion coefficients and higher overpotentials force Li plating [36], an inverse Arrhenius activated behavior is observed for Li plating. This is further supported by a larger exchange current activation energy for Li intercalation compared to Li plating, resulting in increased contributions of the Li plating exchange current at lower temperatures, thus driving Li plating [35].

Notably, one must distinguish between reversible and irreversible Li plating, as reversible Li plating does not contribute to the capacity loss. The amount of irreversibly plated Li increases with decreasing temperature as larger amounts of plated Li growth through the SEI and subsequently react with the electrolyte [36]. This forms a secondary SEI contributing to LLI and thus capacity degradation [36,37]. Furthermore, Li plating is only reversible, as long as the Li is in electrical contact with the anode material. In particular, when stripping the plated Li during discharge, some of the Li may lose contact, resulting in further LLI.

Since SEI growth increases with temperature and Li plating decreases with temperature, the optimum temperature for the longest cycle life lies in between and is defined by the competition of both aging mechanisms [22]. This optimum temperature is determined by the minimum in the Arrhenius plot of the aging rates, which corresponds to the intersection of the low and high temperature branch for Li plating and SEI growth, respectively. Thus, the longest cycle life is achieved at the lowest temperature without Li plating.

The temperature of the minimum aging rate depends on many factors such as the cell chemistry, electrode and cell design, and operating conditions such as charge and discharge rates [6,22,38]. Mostly, 25 °C is quoted as the optimum temperature for cycling Li-ion batteries, however, a wide range of temperatures from 10 °C to 45 °C are reported [6,7, 17,19,39,40].

However, the simplified view of constant temperature aging of Li-ion batteries does not represent typical use-cases. For example, equipment used outdoors is subjected to seasonal temperature variations or a changed temperature after the battery is transferred to a second life application. Indeed, it is still unclear, how changes in temperature affect the cycle life of Li-ion batteries and whether there is a temperature path dependence. For calendar aging at elevated temperatures, Su et al. showed that capacity fade is temperature path independent, i.e. independent of the order of aging at different temperatures [41]. It can therefore be described as a memoryless process. Since calendar aging is a simple Arrhenius activated process for all temperatures [15,21,42], a path independence seems intuitive. However, in general, Li-ion battery aging at different conditions is known be path dependent [43–45]. For example, Raj et al. found an increasing path dependence for alternating calendar and cyclic aging with increasing current load [45].

To best of the author's knowledge, no studies have been reported on the temperature path dependence of cyclic aging at the full temperature operating window of a typical Li-ion battery. A limited number of studies investigates the effect of pre-cycling at a certain temperature on the subsequent aging process, indicating that the first aging can significantly affect the second aging [46–50]. Fig. 1a illustrates how cyclic aging at one temperature, T_1, can impact the subsequent aging at another temperature, T_2. When aging at T_2 follows aging at T_1, it can

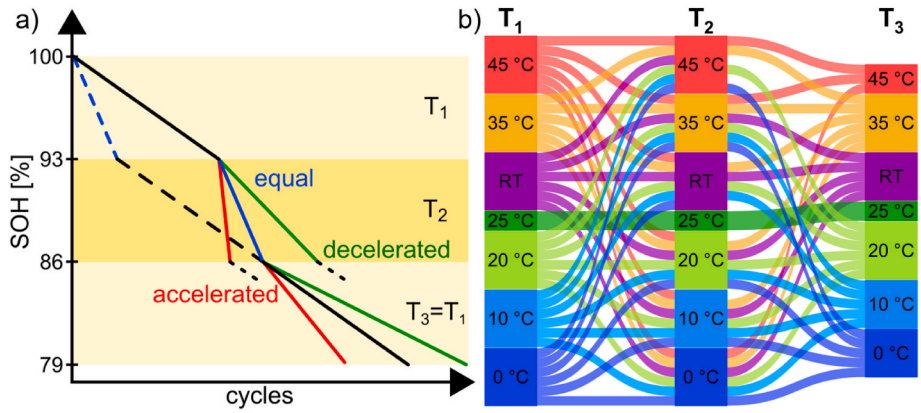

Fig. 1. (a) Depending on the aging at T_1, the aging rate at T_2 can be either equal, accelerated, or decelerated compared to the aging rate without previous aging at T_1 (dashed blue line). Changing the temperature back to T_3, which is equal to T_1, can again result in an equal (black solid line), accelerated (red), or decelerated (green) aging compared to the first aging. (b) Visualization of all aging paths under investigation. Cells were cyclically aged at T_1 and then aged at T_2. The aging of the majority of cells was then continued at T_3, which corresponds to a return to T_1. (For interpretation of the references to color in this figure legend, the reader is referred to the Web version of this article.)

result in one of the three scenarios: the aging at T_2 can be either equal, accelerated, or decelerated compared to the aging at T_2 without prior aging at T_1, i.e. continuously cycling a new cell. If cycling is continued at T_3, which matches T_1, after cycling at T_2, then T_2 can be viewed as an intermittent temperature relative to $T_1 = T_3$. As further shown in Fig. 1a, the aging at T_3 can also be equal, accelerated, or decelerated in comparison to the aging at T_1 due to the intermittent cycling at T_2.

Li plating and SEI growth as the dominant aging mechanisms in the different temperature ranges, are mostly associated with LLI [49]. However, various accompanying degradation processes on electrode level are associated with additional degradation such as loss of anode or cathode active material (LAAM and LCAM) [46,49]. Depending on the degradation mechanisms during first aging, i.e. mostly LLI or LAAM, Li plating becomes more or less likely [51,52]. In particular, previous LLI helps to prevent Li plating since high anode lithiation states are not reached anymore [6,52–54].

To investigate temperature dependent aging mechanisms and aging rates for different previous cyclic aging temperatures, i.e. the temperature path dependence, a large number of cells were cyclically aged following different temperature paths. All temperature paths under investigation, including temperatures in the range of 0 °C–45 °C, are shown in Fig. 1b. While some cells were stopped after the second aging and used for a Post-Mortem analysis, other cells were cycled further at their first aging temperature $T_1 = T_3$. These aging paths with an intermittent aging at T_2 are further shown in Fig. 1b. The temperature changes from T_1 to T_2 and from T_2 to T_3 were performed at 93 % and 86 % state-of-health (SOH), respectively. The end-of-life (EOL) is reached at 79 % SOH. This is typically above the "knee" in the aging trajectory, corresponding to accelerated aging [55].

In addition to evaluating the aging process with Arrhenius plots, Post-Mortem analyses and differential voltage analysis (DVA) were performed to gain further insight into the underlying aging mechanisms and to quantify the contributions of LLI, LAAM, and LCAM. Moreover, 3-electrode full cells with Li reference electrode were reconstructed from a new cell to measure the anode potential vs. Li/Li^+ and provide information on the ability of Li plating, its temperature dependence and behavior during the CV charging phase.

2. Experimental and methods

2.1. Characterization of the commercial pouch cell and Post-Mortem analyses

A commercial Li-ion pouch cell with nominal capacity of 3.3 Ah (12.21 Wh) was used for all tests. The cell, characterized by dimensions of 95 mm × 64 mm × 5.4 mm (L × W × D), has an impedance at 1 kHz of (7.8 ± 0.2) mΩ, measured using a Hioki 3554 battery tester at a delivery voltage of (3.669 ± 0.007) V.

Comprehensive material analyses of the pouch cell, utilizing inductively coupled plasma-optical emission spectroscopy (ICP-OES) using the Spectro Arcos SOP system and scanning electron microscopy (SEM) with energy dispersive X-ray spectroscopy (EDX) using a JEOL IT500, revealed a flaky shaped graphite anode. Further ICP-OES investigations and SEM/EDX mappings of the cathode unveiled a blend of large spherical polycrystalline and small single crystal particles corresponding to $LiNi_{0.756}Co_{0.217}Al_{0.027}O_2$ (NCA) and $LiCoO_2$. The overall stoichiometry was determined to be $LiNi_{0.390}Co_{0.597}Al_{0.013}O_2$. The electrolyte solvent consists of a mixture of EMC and EC, as verified using gas chromatography-mass spectrometry. $LiPF_6$ is used as conductive salt. More detailed insights into the pouch cell and its constituents can be found in Ref. [23].

Aged cells underwent additional ICP-OES assessments to quantify the Li and transition metal (Ni, Co) contents in anode and cathode. Additionally, Mercury intrusion porosity measurements of the electrodes were carried out using a Porotec Pascal 140–440 series apparatus. Details of the method are described by Radloff et al. [56].

2.2. Cyclic aging of the cells

Electrochemical testing, encompassing check-up cycles and cyclic aging, were done using BaSyTec CTS battery test systems. An initial check-up cycle was performed on each cell at room temperature (RT, ~25 °C). Therefore, the cells were discharged (constant current, CC) followed by a charging step (constant current-constant voltage, CC-CV) at a rate of C/10 with a CV phase cut-off current of C/20. The full specified voltage range (2.7 V–4.2 V) results in an average capacity of (3.361 ± 0.012) Ah.

For cyclic aging, the cells were placed in Vötsch climate chambers at constant temperatures of 0 °C, 10 °C, 20 °C, 25 °C, 35 °C, and 45 °C. Additional cells undergoing cycling at RT had no active air circulation and heat up slightly more during operation. As such, RT subsequently denotes the average cell surface temperature of 27 °C.

The cyclic aging of the cells in all phases was performed within the full voltage range by continuous charging (CC-CV) and discharging (CC) with 3 A (~0.91 C for new cells) and a CV cut-off current of C/20. Every 50 cycles a C/10 check-up cycle was done at the aging temperature. A final C/10 check-up cycle was conducted at the aging temperature before transitioning the cell to the next temperature. Owing to concerns about influencing subsequent aging, a check-up at a reference temperature was omitted.

The temperature variations during cyclic aging were done, as shown in Fig. 1a, at 93 % and 86 % SOH. This ensures the same capacity loss of 7 % SOH (~0.23 Ah at RT) during all aging phases. The cyclic aging was stopped after the third aging phase at an SOH of 79 %. The initial discharge cycle at each temperature served as capacity reference for calculation of the relative capacity loss, given that the capacity varies with temperature. Thus, for each aging phase a new initial reference capacity was determined, corresponding to 100 % for T_1, 93 % for T_2 and 86 % SOH for T_3. The end of the aging at T_1 was reached when the capacity loss exceeds 7 %/100 % = 7 % concerning the capacity of the first discharge cycle at T_1. Equivalently, the end of the second and third aging phase was reached, when the capacity loss exceeds 7 %/93 % = 7.53 % and 7 %/86 % = 8.14 %, respectively.

2.3. Reconstruction into 3-electrode full cells with reference electrode

A new pouch cell with initial check-up was used for the reconstruction in a three-electrode setup. Before dismantling the pouch cell in an argon-filled glovebox ($[O_2] < 0.1$ ppm, $[H_2O] < 0.1$ ppm, MBraun), it was fully discharged to 2.7 V in five steps with a C/32 current. The harvested electrodes were washed three times for 1 min in anhydrous DMC (≥ 99 %, Sigma-Aldrich). Following this procedure, the electrodes were dried under vacuum conditions at 3 mbar for 2 h.

While the cell already contains two single-side coated cathodes, there are only double-side coated anodes, which cannot be used in the three-electrode setup. Thus, the anode coating was removed on one side using laser ablation. Subsequently, 18 mm electrodes were punched from of the single-sided anode and cathode in a dry room (dew point < −70 °C).

Three electrode PAT-cells with a Li reference from EL-Cell were subsequently assembled in the glovebox. A double-layer separator (180 µm PP fiber Freudenberg FS2226 E and 38 µm PE membrane Lydall Solupor 5P09B) was used. Else, 100 µl of 1.0 M $LiPF_6$ in EC/EMC (3:7 vol) with 2 wt.-% VC electrolyte from Gotion was inserted into the cell.

After a soaking period of 20 h, three C/10 formation cycles were performed in a CTS climate chamber at 25 °C using a Maccor Series 400 cell test system. The capacity of the reconstructed 3-electrode full cells with Li reference electrode was calculated based on the proportional area of the original pouch cell, resulting in 7.25 mAh. This capacity was used to set a current of 0.91C for the test cycles, ensuring a comparable current density to that of the original pouch cell. The tests were carried out at the same temperatures as before, where 27 °C replicates the RT conditions of the original pouch cell. Intermediate to each test cycle, a C/5 check-up cycle was conducted at 25 °C to facilitate cell recovery.

Furthermore, a C/10 cycle at 25 °C was performed with the reconstructed 3-electrode cells to investigate the single contributions of each electrode in the DVA analysis.

3. Results and discussion

3.1. Cyclic aging at constant temperatures

In order to understand the temperature path dependence of cyclic battery aging, it is essential to first measure the temperature dependent cyclic aging behavior at constant temperatures. To accomplish this, cells were subjected to cyclical aging under various temperatures. The evolution of the capacity over the number of cycles is shown in Fig. 2a. Notably, the lowest aging rate and thus the longest cycle lifespan is observed at 25 °C with 2851 cycles until the EOL at 80 % SOH. As the temperature increases, so does the aging rate, resulting in an EOL at 45 °C after 946 cycles. Conversely, at temperatures below 25 °C, the aging rate increases sharply, leading to an EOL at 0 °C after 23 cycles.

Arrhenius plots are used to better resolve this temperature dependent aging behavior. Therefore, the aging trajectories are fitted linearly (dashed lines in Fig. 2a). The slope of the linear fit for each aging trajectory is defined as the average aging rate *r* for the whole aging process. This aging rate is then plotted logarithmically against the inverse

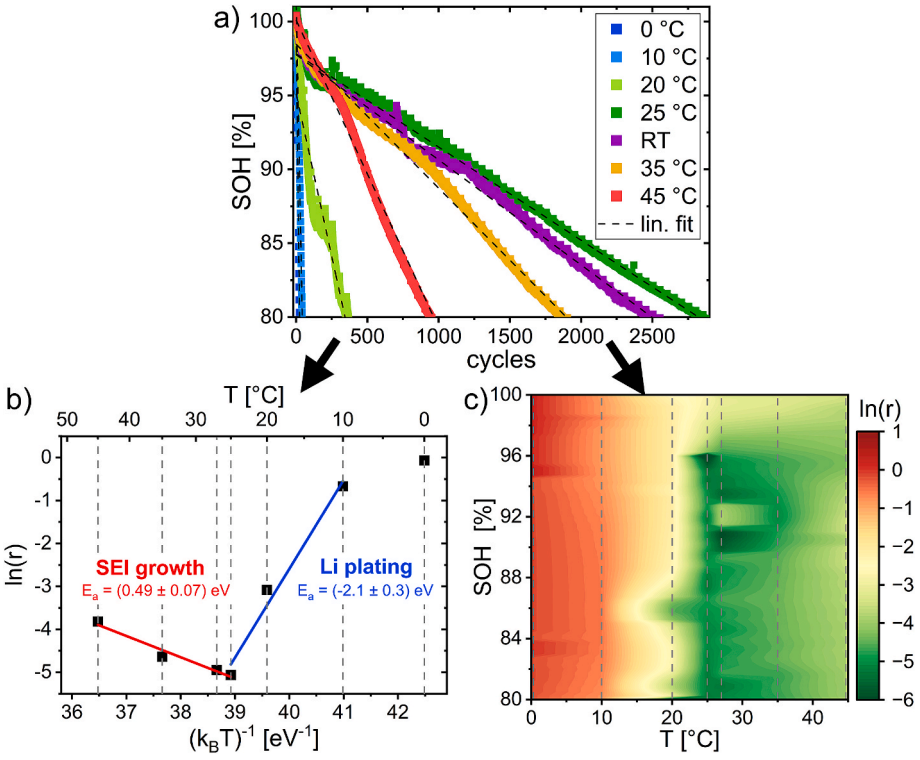

Fig. 2. (a) Aging trajectories of pouch cells aged cyclically at different temperatures. The dashed lines are the linear fit of each aging trajectory. RT corresponds to an average cell temperature of 27 °C. (b) Arrhenius plot of aging rates derived from the linear fits of the aging trajectories. (c) Aging color map derived from the aging trajectories by stepwise calculation of the aging rate to visualize changes in the aging rate during the aging process. (For interpretation of the references to color in this figure legend, the reader is referred to the Web version of this article.)

temperature $(k_B T)^{-1}$ in Fig. 2b to visualize the Arrhenius activated behavior of equation (1). This so called Arrhenius plot shows the expected [4,6,22,23] two branches with Li plating in the low temperature range and SEI growth in the high temperature range. Further linear fitting of the data points for each branch (solid lines in Fig. 2b) gives the activation energy E_a as (-2.1 ± 0.3) eV and (0.049 ± 0.07) eV for the low and high temperature branch, respectively. The high R^2-values (0.979 and 0.965 for low and high temperature fit, respectively) indicate good agreement with the Arrhenius law. The observed activation energies are in a similar range as previously observed for other cells types [4,6,22,23]. The 0 °C data point has not been included in the low temperature branch fit because it does not follow a straight Arrhenius behavior. Including this data point would lead to a R^2-value of 0.891. This will be discussed in more detail in the next section. The lowest aging rate is observed at the intersection of the two branches in the Arrhenius plot at 25 °C, what is consistent with transitions temperatures for Li-ion batteries in literature [4,6,22,23].

Looking more closely at the aging trajectories in Fig. 2a, a greater deviation of the linear fit from the aging trajectory can be seen in particular at the beginning at elevated temperatures. The accelerated capacity loss at the beginning is related to the strong incline of the square root of time and cycles function, which can be used to describe the SEI growth [15,57,58]. This square root of time dependence is well known for calendar aging and mostly coupled with an Arrhenius expression for the temperature dependence [17,26–28,59]. In addition to this SEI growth contribution, cycle induced capacity losses due to particle and SEI cracking with subsequent formation of a new SEI could lead to a capacity fading, which is more linear with the number of cycles [15,17,55]. This leads to typical aging curves lying in the range between linear and square root shaped [15,57,60]. Although the SEI growth dominates with increasing temperature, other cyclic degradation also increases with temperature [6,42].

Concluding, it is almost impossible to find a universal definition of the aging rate from the shape of various aging trajectories due to different degradation mechanisms at different temperatures. To overcome this issue and to further track the changes in the aging rate, aging color plots are introduced here. To create such an aging color map, the related aging trajectories at different temperatures are smoothed by the moving average over 30 cycles (5 cycles for 0 °C and 10 °C aging). Equivalent to the procedure for the standard Arrhenius plot, the aging rate is obtained here by linear fitting of the smoothed curves in 0.25 % SOH increments. In order to cover the wide range of aging rates at different temperatures, the logarithm of the aging rate is plotted through a color-coding as a function of SOH and temperature in the aging color map. Finally, a linear interpolation is made between the studied temperatures to obtain a continuous color plot. The aging color map shown in Fig. 2c is based on the aging trajectories from Fig. 2a. Local variations in the aging rate, such as that seen for 20 °C at 86 % SOH are also visible in the aging color map. This approach is in contrast to the Arrhenius plot in Fig. 2b, where the aging rate is based on average values over the whole cycle life.

As shown in Fig. 2c, the lowest aging rate is shifted as the cell ages. However, temperature has little effect on the aging rate within the first few cycles when no Li plating is observed. While the optimum temperature at the beginning of the aging process in Fig. 2c is observed at 45 °C, it is shifted at around 96 %–97 % SOH to 25 °C, as observed from the averaged aging rates. This raises the question of whether battery life can be extended by following the optimum temperature in Fig. 2c. In order to answer this question, temperature variations were investigated in section 3.3.

3.2. Non-linearity of Li plating branch in Arrhenius plot

The Arrhenius plot in Fig. 2b does not show a straight inverse Arrhenius-activated behavior for the low temperature branch. In order to understand the underlying mechanism, a more detailed evaluation of the charging curves is performed, including measurements with reconstructed 3-electrode full cells with Li reference electrode. Getting an evidence on Li plating by considering the voltage relaxation or the discharge stripping struggles, as the expected Li stripping plateau could not be detected. This is most likely due to insufficiently negative anode potentials [36].

Fig. 3a shows the CC-CV charge voltage curves and applied current for the original pouch cell at various temperatures. At low temperatures, the increasing overpotentials due to limited electrolyte conductivity and sluggish diffusion processes cause the upper voltage limit to be reached more quickly. This results in an extended CV phase and prolonged charging time, even though the total capacity decreases with temperature. Petzl and Danzer detected previously such a behavior [36]. The overpotentials of the full cell are primarily evident in the anode potential, as shown in Fig. 3b by the reconstructed 3-electrode full cell measurements. Three cells were used to reproduce these curves. Notably, the full cell voltage curves of the original pouch cell (Fig. 3a) and the reconstructed cell (Fig. 3b) show good agreement without any capacity loss due to the reconstruction. However, differences in cell format, electrolyte, and separator lead to an increased internal resistance and higher overpotentials. Additionally, charge transfer could be influenced by a modified SEI due to electrode washing and brief air contact of the electrodes in the dry room.

This is further demonstrated in Fig. 3c, where the ratio of the amount charged in the CV charging phase to the total amount charged is plotted against temperature. Apart from the trend of increasing charge ratio in the CV phase at lower temperatures, it is evident that the reconstructed cell consistently shows higher overpotentials compared to the original pouch cell. Consequently, when comparing data from both cell types and correlating the anode potential curves in Fig. 3b with the temperature-dependent aging behavior in Fig. 2, this difference must be taken into account. Larger overpotentials lead to an overestimation of the charge portion charged at negative anode potentials vs. Li/Li^+. This is particularly evident at 25 °C, since the anode potential of the reconstructed 3-electrode full cell obviously becomes slightly negative, but the pouch cell aging behavior as observed by the Arrhenius plot in Fig. 2b suggests no Li plating at 25 °C. Nevertheless, Fig. 3b shows a lower anode potential at lower temperatures, causing it to drop below 0 V vs. Li/Li^+ earlier. At 27 °C and above, the anode potential vs. Li/Li^+ does not become negative for the applied current of 0.91 C. As the current decreases during the CV phase, the overpotentials decrease too, resulting in an increasing anode potential above 0 V vs. Li/Li^+, what is consistent with previous findings [21]. Consequently, a longer CV phase counteracts the favorable conditions for Li plating and chemical intercalation of previously plated Li can occur, supporting the deviation from Arrhenius behavior in Fig. 2b.

Assuming that the aging rate with Li plating as the dominant aging mechanism is proportional to the amount charged at anode potentials below 0 V vs. Li/Li^+, an estimation of the aging rate can be made by considering only the anode potential during charging. Therefore, Fig. 3d shows a pseudo Arrhenius plot of the logarithmic fraction of the capacity charged at negative anode potentials to the total capacity. Remarkably, the shape of this curve aligns well with the low temperature branch of the Arrhenius plot in Fig. 2b, validating the assumption. An absolute prediction of the aging rate from the anode potential is limited by unknown and system-specific parameters such as reintercalation or stripping of the previously plated Li during discharging [61,62].

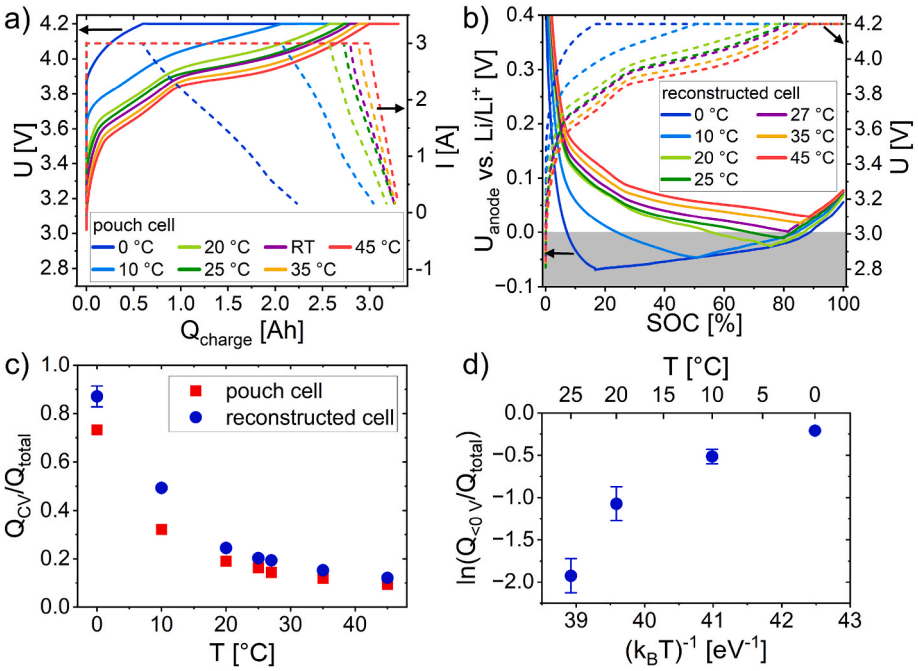

Fig. 3. (a) Charging voltage curves (solid lines) and current (dashed line) for CC-CV charging at different temperatures for the original pouch cell. (b) Anode potential vs. Li/Li^+ (solid lines) and corresponding full cell voltage curves (dashed lines) in reconstructed 3-electrode full cells with Li reference electrode during charging at different temperatures. The region with an anode potential below 0 V vs. Li/Li^+, where Li plating is thermodynamically favored, is marked in grey. (c) Relative amount charged in the CV phase compared to the total charge as a function of temperature for pouch and reconstructed 3-electrode cells. (d) Pseudo Arrhenius plot for the logarithmic fraction of charge charged at an anode potential below 0 V vs. Li/Li^+ relative to the total charge in the reconstructed 3-electrode cell.

3.3. Varying aging temperature and permutability

Depending on the first aging temperature, the subsequent aging process can change significantly. As shown in Fig. 1b, the 36 studied temperature variations are grouped by their six first aging temperatures T_1. For each T_1, the temperature dependent aging behavior in the second phase (93 %–86 % SOH) at T_2 is again evaluated by Arrhenius plots of the aging rate. Fig. 4a–f shows the aging color maps for the aging at various T_2 for the different T_1.

Remarkably, for a T_1 with Li plating as dominant aging mechanism, i.e. $T_1 \leq 20$ °C (Fig. 4a–c), the aging color maps look similar to the map for constant temperature cycling in Fig. 2c for the first 7 % capacity loss. In

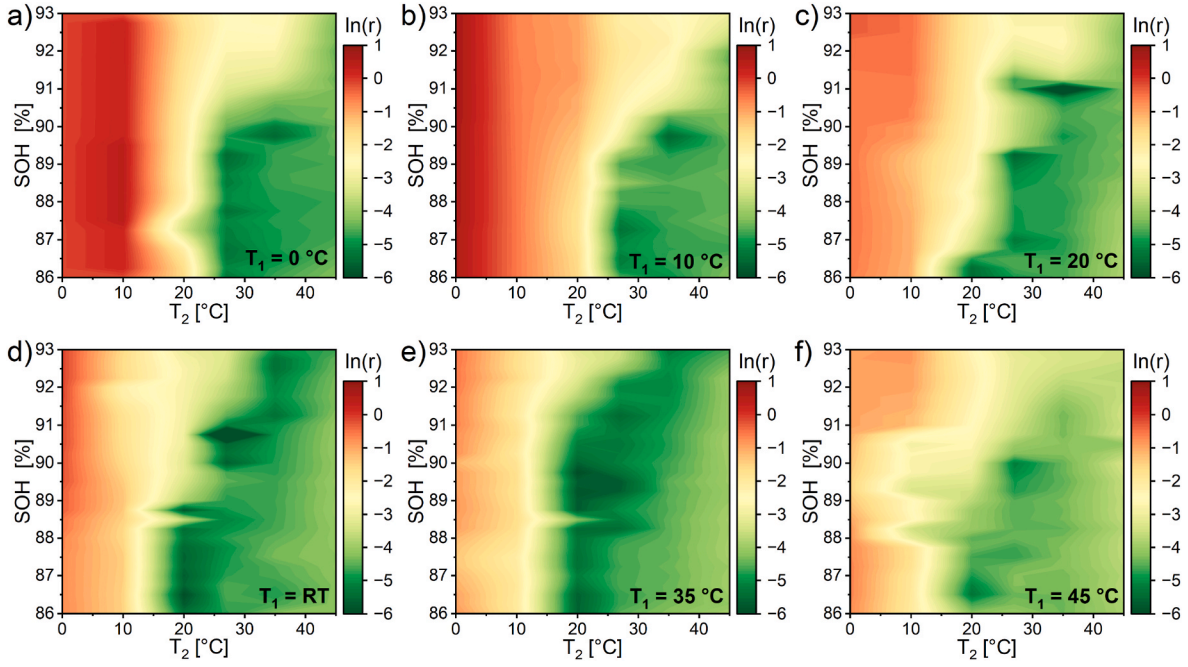

Fig. 4. Aging color maps for the aging in the second phase (93 %–86 % SOH) at T_2 for different previous aging temperatures T_1: (a) 0 °C, (b) 10 °C, (c) 20 °C, (d) RT, (e) 35 °C, and (f) 45 °C. The color indicates the logarithmic aging rate as a function of temperature and SOH. (For interpretation of the references to color in this figure legend, the reader is referred to the Web version of this article.)

particular, the shift of the minimum aging rate to higher temperatures in the first part of the aging process indicates an accelerated SEI growth. Additional contributions could be Li plating induced cracks in the SEI, which are then repaired or a direct reaction of the plated metallic Li with electrolyte [48].

Further low temperature cycling with previous cycling under strong Li plating conditions (0 °C and 10 °C) is characterized by rapid capacity loss. Remarkably, for a $T_1 \geq 20$ °C, the low temperature aging rate decreases, indicated by lighter colors in Fig. 4c–d. As T_1 increases, this effect becomes more pronounced, indicating that Li plating is reduced by previous high temperature cycling. The following DVA confirms LLI during pre-aging at high T_1 which then reduces Li plating in subsequent low temperature aging. A similar effect was recently observed by Flügel et al. for different types of 18,650 cells [52].

Furthermore, Fig. 4d–f shows an extension of the green SEI growth region towards lower temperatures. The lowest aging rate is now achieved at 20 °C, which was previously part of the Li plating branch with much higher aging rates. A first aging at $T_1 = 45$ °C (Fig. 4f) seems to smooth the aging rate, as very high and low rates are shifted towards an intermediate value.

A direct comparison of the different temperature variations and their effect on the cycle life is shown in Fig. 5a. The heat map shows the total number of cycles achieved until an SOH of 86 % for all combinations of T_1 and T_2. Notice the lower left quarter of the heat map with its clear demarcation due to the low number of cycles. This is further confirmed by the Arrhenius plot for the aging rate in T_2 for different T_1 in Fig. 5b. The accelerating nature of Li plating is clearly visible, as pronounced Li plating from the first aging phase accelerates Li plating in the second phase, if the temperature still facilitates Li plating. As can be seen in Fig. 5b for a T_1 of 0 °C and 10 °C, their aging rate for a $T_2 \leq 20$ °C is even higher compared to a new cell without prior aging (grey data points). In contrast, low temperature aging in the second phase is slowed down by previous high temperature cycling. However, a higher T_1 results in lower aging rates for T_2 in the low temperature Li plating range compared to the aging of new cells. As confirmed later by DVA, this is related to a shift in the Li plating onset temperature towards lower temperatures.

As Fig. 5a further shows, the longest cycle life until 86 % SOH is achieved for medium T_1 and T_2. More specifically, the longest cycle life is observed for a first aging at RT and a second aging at 20 °C with a total of 1885 cycles. A first aging at 35 °C and second aging at 20 °C still gives a very long cycle life of 1807 cycles. This is even longer than the constant temperature cycling at RT with 1668 cycles. Considering the number of cycles achieved at $T_2 = 20$ °C, almost 250 cycles are achieved more at $T_1 = 35$ °C than at RT, as the aging after $T_1 =$ RT has an accelerated aging at the beginning of the second phase which could not be seen for $T_1 = 35$ °C (see Fig. 4d and e). This effect is not visible anymore in the total number of cycles in Fig. 5a, because of the obviously lower aging rate at $T_1 =$ RT than for 35 °C.

This improved lifetime by changing the temperature from RT or 35 °C cycling to 20 °C is clearly visible in Fig. 5b by the new global minimum. 20 °C now belongs to the SEI growth branch, which goes along with a shift of the Li plating onset temperature towards lower temperatures. As Li plating is known to have a strong temperature dependence and typically a much higher aging rate than SEI growth (see Fig. 2b), the drastically lowered aging rate follows.

The main driver for the Li plating onset shift, as later confirmed by DVA, is LLI. However, the increasing internal resistance during cell aging leads to increased polarization and thus may compete with the shift of the Li plating onset towards lower temperatures. Thus, the less pronounced Li plating onset shift at $T_1 = 45$ °C (see Fig. 5b) could be a result of the greater increase in internal resistance, as the changes in LLI are minimal compared to the changes in the internal resistance (determined by the IR-drop).

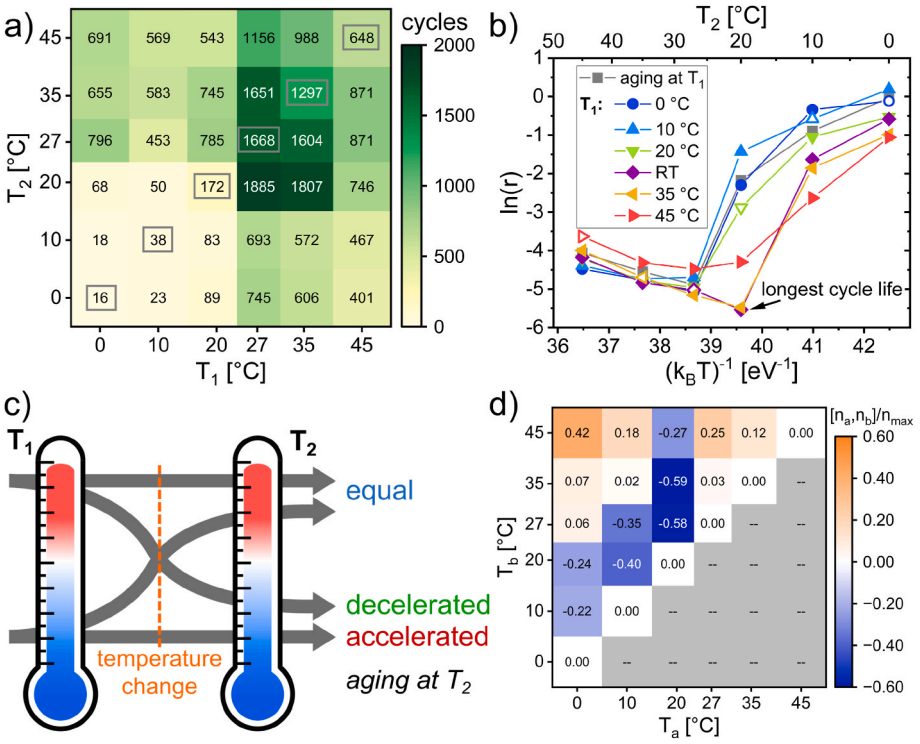

Fig. 5. (a) Heat map of for the total number of cycles to 86 % SOH after cycling at T_1 and T_2. Grey boxes mark constant temperature cycling. (b) Arrhenius plot for aging at T_2 for different T_1. 'Aging at T_1' marks the temperature dependent aging rate for the aging in the first phase of a new cell. Open symbols mark the reference value for cycling at constant temperature and lines are added to guide the eye. (c) Schematic summary of the four main temperature paths leading to equal, accelerated, or decelerated aging at T_2 compared to the aging of a new cell. (d) Heat map of the commutator $[n_a, n_b]$ normalized to n_{max} to evaluate the permutability of the aging at two temperatures T_a and T_b. Permutability is given for $[n_a, n_b]/n_{max} = 0$.

The second aging in the high temperature range seems to be only slightly influenced by the previous aging temperature. There is only a slight tendency towards higher aging rates with higher T_1 visible, especially for $T_1 = 45$ °C.

These findings are summarized in four main temperature paths in Fig. 5c, as the aging rate at T_2 can be equal, accelerated, or decelerated compared to the aging of a new cell. As suggested above to follow the optimum temperature in the color map of Fig. 2c does not result in a superior life. A temperature change at 97 % SOH from 45 °C to RT results in 1683 cycles until the SOH reaches 86 %, which is comparable to constant temperature cycling at RT.

So far we have shown that changing the temperature during cyclic aging can largely alter the cycle life of batteries. Using the observed temperature dependent aging rates of fresh cells to estimate the aging after a temperature variation mostly fails because the aging at T_2 can significantly differ dependent on T_1. This raises the question of when, or under which conditions, aging at two temperatures is permutable and therefore path independent. To address this mathematically, the commutator is used. It is defined for two operators x and y by [63]

$$[x, y] = xy - yx. \tag{2}$$

If x and y commute, it follows that $xy = yx$ and hence $[x, y] = 0$. Applied to the aging process of batteries at two different temperatures T_a and T_b, these operators refer to the number of cycles $n_{T,i}$ at a given temperature $T \in \{a, b\}$ in the first or second phase $i \in \{1, 2\}$. Thus, the permutability for the aging at two temperatures can be described by

$$[n_a, n_b] = \left(n_{a,1} + n_{b,2}\right) - \left(n_{b,1} + n_{a,2}\right) \tag{3}$$

with the sums of the cycles in the first and second temperature phases for each direction. As the number of cycles between different aging paths largely varies, the commutator is normalized by the maximum number of cycles

$$n_{\max} = \max\left\{\left(n_{a,1} + n_{b,2}\right), \left(n_{b,1} + n_{a,2}\right)\right\} \tag{4}$$

for a pair of temperatures. This normalized commutator is then applied to all pairs of aging temperatures and shown in a heat map in Fig. 5d. $T_a \leq T_b$ is chosen for the plot.

The empty part of the heat map contains all the inverted values mirrored on the diagonal. The more $[n_a, n_b]/n_{\max}$ deviates from 0 (white in Fig. 5d), the worse is the permutability of the aging at two temperatures. On the diagonal, where the temperature is not varied, the commutator is by definition zero. Values < 0 (blue) in Fig. 5d show that the change from T_b to T_a is more advantageous and vice versa values $>$ 0 (orange) show that the change from T_a to T_b is more advantageous for maximizing cycle life.

Fig. 5d reveals that the permutability of cyclic aging at different temperatures can be very complex as it depends on many factors. If SEI growth is the dominant aging mechanism for both aging phases ($\geq$ RT), there is approximately no path dependence. The accelerating nature of Li plating is seen indirectly in the permutability at low temperatures, as existing Li plating from previous low temperature cycling accelerates the subsequent Li plating, resulting in limited permutability.

Even though first high temperature cycling shifts the onset of Li plating and reduces the Li plating at a given temperature, the aging rate of Li plating was still orders of magnitude higher than for SEI growth. Since Li plating from the first aging phase does not significantly affect the subsequent high temperature aging, there is a good permutability given, even if the aging mechanism is different for both temperatures.

The change in the dominant aging mechanism from Li plating to SEI growth at 20 °C after previous aging at RT or 35 °C results in the strongest path dependence, as a new cell ages comparatively fast at 20 °C.

It is also noteworthy that the permutability of 45 °C with 0 °C in particular is very poor in Fig. 5d. Fig. 4 provides a possible explanation, as especially the second aging at 45 °C is more constant than the aging at other elevated temperatures. Thus, even compared to the first aging, the cycle life at $T_2 = 45$ °C is increased due to the slow aging rate starting right at the beginning.

3.4. DVA of cells with temperature variation

So far, the aging behavior under different temperature paths has been analyzed, but not fully explained. Therefore, DVA of all cells in the first and second temperature phase were performed to reveal the underlying aging mechanisms. DVA is a well-known tool for investigating aging mechanisms by separating anode and cathode contributions in full cells and shifts in the electrode balancing [13].

DVA requires small currents, as the peaks for evaluation become increasingly blurred with higher currents. Therefore, the C/10 CC charge step from the check-up cycles were used. First, the raw voltage data U was smoothed and then derived after the charge Q for the DVA. The DVA of the reconstructed 3-electrode full cells with Li reference electrode at 25 °C is shown in Fig. 6a. The Li reference electrode allows measuring individual electrode potentials and therefore separate DVA of the anode and cathode can be made to differentiate between anode and cathode peaks. According to Keil and Jossen, two peaks, labelled as 'I' and 'II' in Fig. 6a, and the charge start and end points are used to determine the aging contributions [13]. The peak at around 20 % state-of-charge (SOC) cannot be used for evaluation as the anode and cathode peaks overlap. Q_1 is defined by the capacity between 0 % SOC, representing an empty anode, and anode peak I and thus provides information on the available anode capacity. The capacity from peak I to 100 % SOC is defined as Q_2. As the end of charge is defined by an increasing cathode potential, Q_2 relates an anode to a cathode characteristic and therefore gives an indication on the balancing of the electrodes. Typically, peak I, dividing the total capacity into Q_1 and Q_2, is referred as the central graphite peak at around 55 %–80 % SOC, where the transition from the medium to the lower anode potential plateau occurs [13]. As can be seen in Fig. 6a, Q_1 is much larger than Q_2 indicating a large negative/positive (n/p) electrode areal capacity ratio, which helps to increase the cycle life [64]. The capacity between the cathode peak II and 100 % SOC is defined as Q_3. Analogous to Q_1 for the anode, Q_3 correlates two cathode characteristics and therefore provides information on the available cathode capacity.

The DVA is now applied to the first aging phase in Fig. 6b to reveal the effect of the cycling temperature on the degradation mechanism. The changes in Q_1, Q_2, and Q_3 from the initial (Q_{start}) to the final (Q_{end}) check-up of the aging phase are normalized to the total capacity loss by

$$\frac{\Delta Q_i}{\Delta Q_{\text{total}}} = \frac{Q_{i,\text{start}} - Q_{i,\text{end}}}{Q_{\text{start}} - Q_{\text{end}}} \tag{5}$$

for each Q_i where $i \in \{1, 2, 3\}$. The total capacity loss is always 7 %, but the absolute capacity values differ due to temperature dependent capacities.

Remarkably, the two dominant aging mechanisms for the low and high temperature range observed in the Arrhenius plot (Fig. 2b) are again found in Fig. 6b. While Q_3 is close to zero for all temperatures, indicating no cathode degradation, Q_1 and Q_2 change significantly with temperature and aging mechanism. Li plating in the low temperature range reduces the available anode capacity, as Q_1 is the almost only contributor to the capacity loss. This could either be a result of LAAM or a passivation of the plated Li by reactions with the electrolyte resulting in pore clogging [22,46,55,65]. Although this reduces the anode capacity and minor contributions from Q_2, indicating no LLI, lead to a shift in the n/p ratio. However, due to the large anode capacity overhang, the Li plating capability is most likely minor affected. Nevertheless, pore clogging could lead similar to LAAM to locally increased current densities, triggering further Li plating, even if the remaining anode capacity is not limiting [49,55,66]. This is further supported by a strongly increasing internal resistance after low temperature cycling. Coron et al. showed that even if large LAAM has

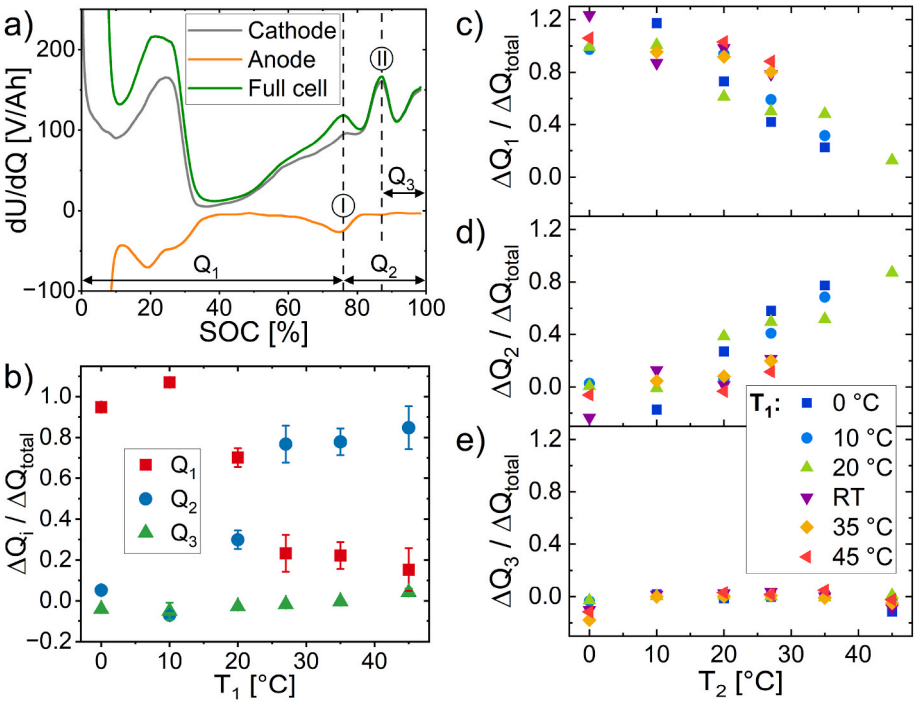

Fig. 6. (a) Exemplary DVA of the reconstructed 3-electrode full cells with Li reference electrode for anode, cathode, and full cell potential. The characteristic anode and cathode peaks used to define Q_1, Q_2, and Q_3 are indicated by 'I' and 'II' (b) Proportion of capacity loss due to Q_1, Q_2, and Q_3 related to the total capacity loss as a function of temperature for the first aging phase. Proportions of capacity loss for (c) Q_1, (d) Q_2, and (e) Q_3 relative to the total capacity loss during cyclic aging at T_2 for different T_1.

occurred after cycling with Li plating, the subsequent aging is not further affected [46]. This is consistent with our findings for a second aging phase at elevated temperatures (see Fig. 5b).

In contrast, Petzl et al. determined LLI using DVA as the main contributor to the capacity loss at low temperature [54]. However, they observed a partial reversibility of the capacity loss during cycling at 25 °C after previous Li plating, whereas Fig. 4a–c shows no reversible capacity after Li plating. This suggests different effects at the electrode level, at least beyond possible reintercalation.

As the temperature is increased, Q_1 and Q_2 change position and Q_2 becomes the dominant contributor. The anode degradation, observed by Q_1, contributes approximately 20 % to the total capacity loss and decreases slightly with temperature. Consistently, Q_2 and therewith LLI increases in the same way. The number of cycles until 93 % SOH decreases with increasing temperature because the side reactions with LLI become more pronounced. As the cyclic degradation of the anode is mainly triggered by particle and SEI cracking due to volume changes during cycling, a higher number of cycles at lower temperatures leads to an increased contribution of LAAM (Q_1), as the graphite particles are typically lost in a rather delithiated state triggering low LLI [65]. The large LLI in combination with small LAAM and LCAM correlate with a reduced utilization of both electrodes [13]. Consequently, the now even more oversized anode reduces the ability for Li plating, leading to a shift in the onset of Li plating towards lower temperatures.

DVA is carried out in the same way for the second aging phase. As high temperature aging favors large contributions from Q_2, the distance between the peaks I and II becomes too small to distinguish between the peaks. Therefore some data points are missing in Fig. 6c–e.

The contributions of Q_1 and Q_2 (Fig. 6c and d) to the total capacity loss follow a similar temperature trend as observed in the first aging phase in Fig. 6b. However, the transition from the low to the high temperature range is smoother and a higher temperature dependency is observed especially in the high temperature range. In addition, Fig. 6c and d shows the trend that a lower T_1, i.e. more pronounced Li plating, results in a greater contribution of LLI and thus a smaller LAAM. Furthermore, it appears that at medium temperatures, especially after previous cycling without Li plating, LAAM dominates over LLI. This could be explained by the square root of time dependence of the SEI growth, i.e. the Li consumption by SEI growth decreases with time. If a low T_1 limited the SEI growth, this is compensated for in the second aging phase, as already shown in Fig. 4. Fig. 6e shows that there is similar to the aging at T_1 no LCAM for all T_2.

3.5. Post-Mortem analyses of cells with temperature variation

To gain further insight into the aging mechanism, Post-Mortem analyses of cells after the second aging phase and of a new cell for comparison were performed. Visual inspection of all aged cells confirmed a good condition of the electrodes at an SOH of 86 %. The adhesion of the active material to the metal foil was still good and only small Li depositions at the edges of the anodes were found for some cells. For cells after low temperature aging, a very thin layer of plated Li was observed on the anode surface. In addition, all cells showed an excess of electrolyte.

The accumulated porosity of the determined pore size distribution for anode and cathode in Fig. 7a show minor changes with aging. An exception is the value of the temperature combination RT - 0 °C, which is most likely an outlier. However, an increase in porosity due to particle cracking could be excluded by additional pore clogging.

The coating thickness was determined by measuring the thickness of the double-side coated electrode and current collecting foil with a micrometer gauge and dividing the difference in thickness in half. As shown in Fig. 7b, the coating thickness of anode of the aged cells increases particularly slightly. The small thickness change even after low temperature cycling indicates only a small amount of plated Li on the surface. Again, there is no trend for a temperature aging path dependence visible as the changes are small.

The Li content in the fully discharged state in anode and cathode, measured by ICP-OES, is shown in Fig. 7c. In theory, the sum of the anode and cathode should be constant. However, the washing process of the electrodes could have affected this parameter, e.g. by washing out

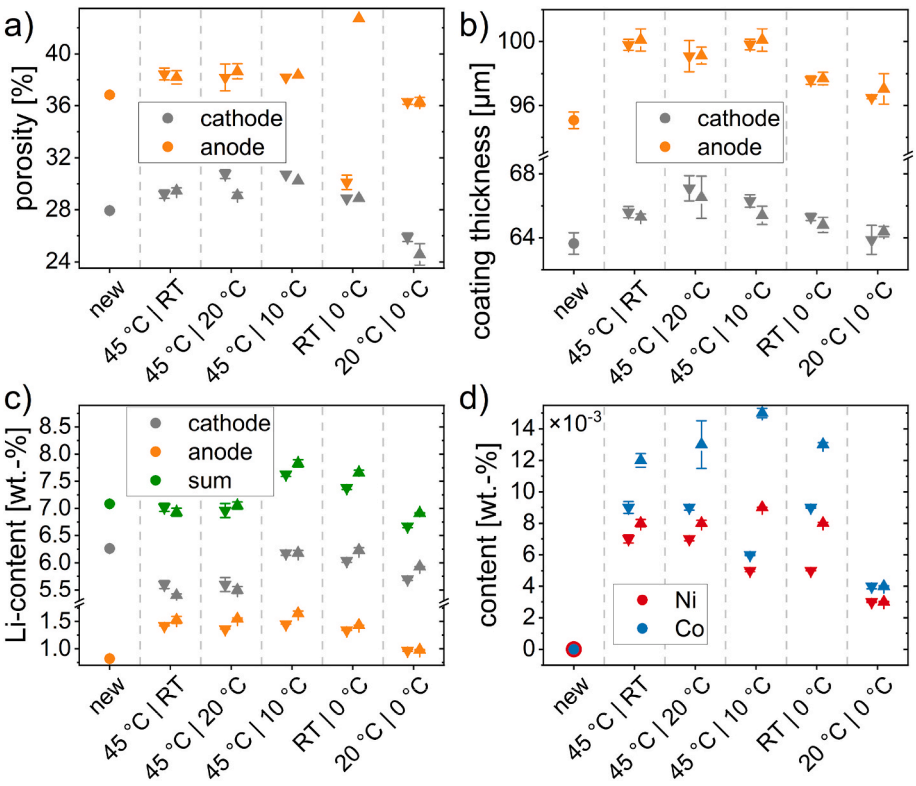

Fig. 7. Post-Mortem analyses of selected temperature variation cells for both directions of an aging path. The circular data points represent the values for the new cell. Triangles represent the aged cell, where an upward triangle corresponds to the change from a lower to a higher temperature and vice versa for a downward triangle. (a) Mercury intrusion porosity values, (b) coating thickness, (c) Li content measured by ICP-OES for both anode and cathode, and (d) Ni and Co content in the anode, measured by ICP-OES.

some of the Li containing SEI, or by a changed solubility due to aging and corresponding Li-ion concentration of the removed electrolyte. Nevertheless, it is evident that the amount of irreversibly bound Li in the anode has increased, particularly for the aging paths involving elevated temperatures. As the SOH of all cells was very similar and DVA confirmed similar aging mechanisms for these cells, a similar Li content is obvious. Otherwise, the 20 °C–0 °C aging path shows almost no irreversibly bound Li in the anode, confirming the loss of anode active material as the main aging mechanism, as previously predicted by DVA.

Dissolution of cathode active material is known to be a significant contributor to capacity loss, particularly for Mn-containing cathodes [10,17,67,68]. The transition metals are dissolved from the cathode, migrate to the anode and become reduced causing a ticker and less uniform SEI [69]. As the cathode contains no Mn, the ICP-OES measurements in Fig. 7d show only small amounts of Ni and Co in the anode after aging. These low levels of dissolved transition metals confirm the DVA results that the cathode does not degrade significantly. Remarkably, the change from lower to higher temperatures in Fig. 7d shows a consistently higher value for Ni and Co in the anode. This is most likely an effect of time and number of cycles. It is also conceivable that a previous aging facilitates the transition metal dissolution, which is known to occur particularly at elevated temperatures.

3.6. Intermittent temperature variation

If the temperature is changed back to the $T_1 = T_3$ after the second aging, T_2 can be considered as an intermittent aging temperature. The intermittent temperature aging is defined by a capacity loss of 7 % SOH. Fig. 8 shows the aging rate after intermittent temperature cycling for different T_3 as a function of T_2. The constant temperature cycling without intermittent temperature change is used as a reference (empty symbols in Fig. 8).

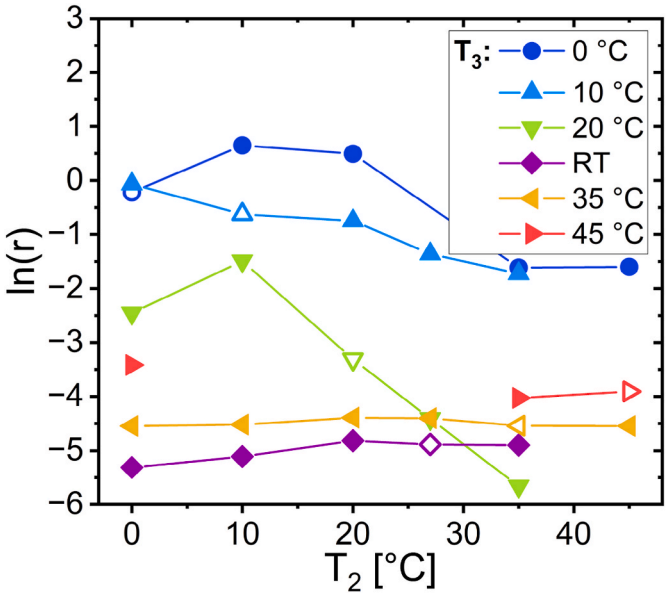

Fig. 8. Aging rate for different T_3 corresponding to T_1 as a function of T_2. Open symbols mark the reference value for cycling at constant temperature. Lines are added to guide the eye.

The already discussed effects of temperature changes on the aging rate and dominant aging mechanisms, help to understand the effect of the intermittent temperature in Fig. 8. Again, it can be seen, that Li plating is accelerated for previous cycling at even lower temperatures with more pronounced Li plating. On the other hand, if aging was previously carried out at elevated temperatures, the subsequent aging

under Li plating conditions will be slower. Fig. 8 confirms the trend that a higher intermittent temperature leads to a greater deceleration of Li plating.

For high temperature aging, the effect of the intermittent temperature is rather small as the aging rate does not change much. For $T_3 = RT$ and 35 °C, a low intermittent temperature of 0 °C or 10 °C seems to slightly slow down the aging. This could be an effect of the much lower cycle number and therefore shorter time at the intermittent temperature, leading to less other accompanying aging mechanisms.

Aging at 20 °C again plays a special role due to the change in aging mechanism after high temperature cycling. While a lower intermittent temperature leads to accelerated aging, a higher aging temperature, and in particular 35 °C, significantly reduces the aging rate. The 7 % capacity loss during this 35 °C aging is sufficient to shift the onset of Li plating below 20 °C, therefore dramatically increasing the battery life.

4. Conclusions

A total of 36 temperature aging paths in the range of 0 °C–45 °C were investigated by cyclic aging of commercial Li-ion pouch cells. For constant temperature aging, which is used as a reference, a minimum aging rate is observed at 25 °C in an Arrhenius plot. This minimum corresponds to the transition from Li plating (dominating the low temperature range) to accelerated SEI growth (dominating the high temperature range). However, Li plating is much more temperature sensitive than SEI growth, resulting in much faster capacity degradation.

Newly introduced aging color maps for the constant temperature cycling visualize changes in the aging rate. Thereby, an accelerated degradation and shift of the optimum temperature towards higher temperatures at the beginning of the aging process is found. A clear Arrhenius behavior was confirmed for the SEI growth. In contrast, Li plating showed an increasing deviation from the inverse Arrhenius behavior with decreasing temperature. This can be explained by the decreasing current in the extended CV phase at low temperatures. Reconstructed 3-electrode full cells with Li reference electrode showed an increasing anode potential during the CV phase even above 0 V vs. Li/Li^+, i.e. a long CV phase counteracts Li plating conditions. The estimated amount of charge under Li plating conditions is in good agreement with the Arrhenius plot of aging rates.

Based on the combination of the two dominant aging mechanisms, Li plaiting and SEI growth, the impact of changing the temperature and potentially changing the aging mechanism on the aging rate can be grouped into four characteristic cases (see Fig. 5c):

- First aging at low temperature ($\leq$ 20 °C) under Li plating condition accelerates Li plating during the second aging at low temperature.
- First aging with Li plating does not significantly affect subsequent aging at high temperature ($\geq$ RT $\triangleq$ 27 °C).
- First high temperature aging with accelerated SEI growth has little effect on subsequent elevated temperature aging.
- First aging at high temperature reduces Li plating during subsequent low temperature aging.

DVA of the first aging phase shows that SEI growth is largely dominated by LLI with minor contributions from LAAM. Thus, the onset of Li plating is shifted to lower temperatures because higher critical intercalation states in the anode are prevented. As a result, aging first at RT or 35 °C and secondly at 20 °C dramatically increases cycle life by changing the dominant aging mechanism from Li plating to SEI growth. As the SEI growth rate at 20 °C is lower than at RT, the total number of cycles observed on the RT–20 °C and 35 °C–20 °C path is even higher than for continuous cycling at RT, i.e. a new global minimum aging rate is reached. It should be noted, that the results from this study may differ for other dominant degradation mechanisms in other cell types. For example, additional Silicon compounds in the anode can lead to more LAAM, making Li plating even more likely [52]. Furthermore, lowering the charging C-rate or carefully designing the charging protocols in particular for the second aging phase could further optimize the aging rate by shifting the onset of Li plating to even lower temperatures.

Describing the path dependence for cyclic aging at different temperatures can be complex, because the characteristic cases of temperature changes are not reversible. In general, the closer two temperatures are, the better the permutability. However, a changing aging mechanism, such as that observed at 20 °C after previous high temperature cycling, limits the permutability. In addition, pronounced Li plating during first aging could accelerate subsequent Li plating. Similar to calendar aging [41], if SEI growth is the dominant aging mechanism at both temperatures, there is also no path dependence for cyclic aging.

Interrupting the constant temperature cycling with an intermittent temperature change, results in a similar behavior. Cyclic aging at high temperatures is barely affected by intermittent temperature cycling. Low temperature aging in particular shows a reduced aging rate after an intermittent cycling at elevated temperatures, which is again pronounced for the aging at 20 °C.

As the investigations show, the dominant aging mechanisms are associated with aging on the anode side and the NCA cathode is only slightly affected. It can therefore be assumed that the results can be transferred to other cathode materials, provided their cycling stability is comparable to that of NCA.

In summary, this study provides valuable information on how cycling a battery at different temperatures affects the subsequent aging. It turns out that a simple relation with SOH is not sufficient to estimate the subsequent aging rate, as battery aging cannot be considered as a memoryless process in general. Therefore, it is very important to consider the previous aging temperature and aging mechanism, e.g., when selecting a battery for re-use in second life applications and its operating conditions. Furthermore, our results might be helpful for battery aging models with temperature variation, as simple temperature dependent aging rates can lead to large discrepancies.

CRediT authorship contribution statement

Max Feinauer: Conceptualization, Methodology, Software, Validation, Investigation, Data curation, Writing – original draft, Visualization. **Margret Wohlfahrt-Mehrens:** Resources, Writing – review & editing, Supervision, Project administration, Funding acquisition. **Markus Hölzle:** Resources, Writing – review & editing, Supervision. **Thomas Waldmann:** Conceptualization, Methodology, Validation, Resources, Writing – review & editing, Supervision, Project administration, Funding acquisition.

Declaration of competing interest

The authors declare that they have no known competing financial interests or personal relationships that could have appeared to influence the work reported in this paper.

Data availability

Data will be made available on request.

Acknowledgement

We gratefully acknowledge the German Federal Ministry of Education and Research (BMBF) for the financial support of the projects MiCha (03XP0317C), CharLiSiKo (03XP0333A), and AnaLiBa (03XP0347C) within the AQua cluster, the German Federal Ministry of Economic Affairs and Climate Action (BMWK) for funding of the project CIRCULUS (03ETE035F), as well as project management by the Projektträger Jülich (PtJ). We thank the ZSW members A. Aracil Regalado, B. Anglet, G. Arnold, and K. Fischinger for their support in Post-Mortem analyses.

References

[1] J.T. Frith, M.J. Lacey, U. Ulissi, Nat. Commun. 14 (2023) 420, https://doi.org/10.1038/s41467-023-35933-2.
[2] Y. Ding, Z.P. Cano, A. Yu, J. Lu, Z. Chen, Electrochem. Energy Rev. 2 (2019) 1–28, https://doi.org/10.1007/s41918-018-0022-z.
[3] B.Y. Liaw, E. Roth, R.G. Jungst, G. Nagasubramanian, H.L. Case, D.H. Doughty, J. Power Sources 119–121 (2003) 874–886, https://doi.org/10.1016/S0378-7753(03)00196-4.
[4] T. Waldmann, M. Wilka, M. Kasper, M. Fleischhammer, M. Wohlfahrt-Mehrens, J. Power Sources 262 (2014) 129–135, https://doi.org/10.1016/j.jpowsour.2014.03.112.
[5] M. Ecker, N. Nieto, S. Käbitz, J. Schmalstieg, H. Blanke, A. Warnecke, D.U. Sauer, J. Power Sources 248 (2014) 839–851, https://doi.org/10.1016/j.jpowsour.2013.09.143.
[6] G. Kucinskis, M. Bozorgchenani, M. Feinauer, M. Kasper, M. Wohlfahrt-Mehrens, T. Waldmann, J. Power Sources 549 (2022), 232129, https://doi.org/10.1016/j.jpowsour.2022.232129.
[7] A. Friesen, X. Mönnighoff, M. Börner, J. Haetge, F.M. Schappacher, M. Winter, J. Power Sources 342 (2017) 88–97, https://doi.org/10.1016/j.jpowsour.2016.12.040.
[8] Y. Wu, P. Keil, S.F. Schuster, A. Jossen, J. Electrochem. Soc. 164 (2017) A1438–A1445, https://doi.org/10.1149/2.0401707jes.
[9] J. Vetter, P. Novák, M.R. Wagner, C. Veit, K.-C. Möller, J.O. Besenhard, M. Winter, M. Wohlfahrt-Mehrens, C. Vogler, A. Hammouche, J. Power Sources 147 (2005) 269–281, https://doi.org/10.1016/j.jpowsour.2005.01.006.
[10] M.M. Kabir, D.E. Demirocak, Intl J of Energy Research 41 (2017) 1963–1986, https://doi.org/10.1002/er.3762.
[11] T. Waldmann, A. Iturrondobeitia, M. Kasper, N. Ghanbari, F. Aguesse, E. Bekaert, L. Daniel, S. Genies, I.J. Gordon, M.W. Löble, E. de Vito, M. Wohlfahrt-Mehrens, J. Electrochem. Soc. 163 (2016) A2149–A2164, https://doi.org/10.1149/2.1211609jes.
[12] P. Keil, S.F. Schuster, J. Wilhelm, J. Travi, A. Hauser, R.C. Karl, A. Jossen, J. Electrochem. Soc. 163 (2016) A1872–A1880, https://doi.org/10.1149/2.0411609jes.
[13] P. Keil, A. Jossen, J. Electrochem. Soc. 164 (2017) A6066–A6074, https://doi.org/10.1149/2.0091701jes.
[14] S. Käbitz, J.B. Gerschler, M. Ecker, Y. Yurdagel, B. Emmermacher, D. André, T. Mitsch, D.U. Sauer, J. Power Sources 239 (2013) 572–583, https://doi.org/10.1016/j.jpowsour.2013.03.045.
[15] J. Schmalstieg, S. Käbitz, M. Ecker, D.U. Sauer, J. Power Sources 257 (2014) 325–334, https://doi.org/10.1016/j.jpowsour.2014.02.012.
[16] Y. Cui, C. Du, G. Yin, Y. Gao, L. Zhang, T. Guan, L. Yang, F. Wang, J. Power Sources 279 (2015) 123–132, https://doi.org/10.1016/j.jpowsour.2015.01.003.
[17] J. Wang, J. Purewal, P. Liu, J. Hicks-Garner, S. Soukazian, E. Sherman, A. Sorenson, L. Vu, H. Tataria, M.W. Verbrugge, J. Power Sources 269 (2014) 937–948, https://doi.org/10.1016/j.jpowsour.2014.07.030.
[18] R. Gauthier, A. Luscombe, T. Bond, M. Bauer, M. Johnson, J. Harlow, A. Louli, J. R. Dahn, J. Electrochem. Soc. 169 (2022), 20518, https://doi.org/10.1149/1945-7111/ac4b82.
[19] Z. Gao, H. Xie, X. Yang, W. Niu, S. Li, S. Chen, Batteries 8 (2022) 234, https://doi.org/10.3390/batteries8110234.
[20] P.W. Atkins, in: Physical Chemistry, 4, Oxford University Press, Oxford, 1990.
[21] T. Waldmann, M. Kasper, M. Wohlfahrt-Mehrens, Electrochim. Acta 178 (2015) 525–532, https://doi.org/10.1016/j.electacta.2015.08.056.
[22] X.-G. Yang, C.-Y. Wang, J. Power Sources 402 (2018) 489–498, https://doi.org/10.1016/j.jpowsour.2018.09.069.
[23] M. Feinauer, A.A. Abd-El-Latif, P. Sichler, A. Aracil Regalado, M. Wohlfahrt-Mehrens, T. Waldmann, J. Power Sources 570 (2023), 233046, https://doi.org/10.1016/j.jpowsour.2023.233046.
[24] S.J. An, J. Li, C. Daniel, D. Mohanty, S. Nagpure, D.L. Wood, Carbon 105 (2016) 52–76, https://doi.org/10.1016/j.carbon.2016.04.008.
[25] R. Li, S. O'Kane, M. Marinescu, G.J. Offer, J. Electrochem. Soc. 169 (2022), 60516, https://doi.org/10.1149/1945-7111/ac6f84.
[26] I. Bloom, B. Cole, J. Sohn, S. Jones, E. Polzin, V. Battaglia, G. Henriksen, C. Motloch, R. Richardson, T. Unkelhaeuser, D. Ingersoll, H. Case, J. Power Sources 101 (2001) 238–247, https://doi.org/10.1016/S0378-7753(01)00783-2.
[27] M. Broussely, S. Herreyre, P. Biensan, P. Kasztejna, K. Nechev, R.J. Staniewicz, J. Power Sources 97–98 (2001) 13–21, https://doi.org/10.1016/S0378-7753(01)00722-4.
[28] H.J. Ploehn, P. Ramadass, R.E. White, J. Electrochem. Soc. 151 (2004) A456, https://doi.org/10.1149/1.1644601.
[29] I. Bloom, S.A. Jones, E.G. Polzin, V.S. Battaglia, G.L. Henriksen, C.G. Motloch, R. B. Wright, R.G. Jungst, H.L. Case, D.H. Doughty, J. Power Sources 111 (2002) 152–159, https://doi.org/10.1016/S0378-7753(02)00302-6.
[30] B. Heidrich, M. Stamm, O. Fromm, J. Kauling, M. Börner, M. Winter, P. Niehoff, J. Electrochem. Soc. 170 (2023), 10530, https://doi.org/10.1149/1945-7111/acb401.
[31] T. Waldmann, B.-I. Hogg, M. Wohlfahrt-Mehrens, J. Power Sources 384 (2018) 107–124, https://doi.org/10.1016/j.jpowsour.2018.02.063.
[32] M. Angeles Cabañero, J. Altmann, L. Gold, N. Boaretto, J. Müller, S. Hein, J. Zausch, J. Kallo, A. Latz, Energy 171 (2019) 1217–1228, https://doi.org/10.1016/j.energy.2019.01.017.
[33] J. Fan, S. Tan, J. Electrochem. Soc. 153 (2006) A1081, https://doi.org/10.1149/1.2190029.
[34] L.W. Juang, P.J. Kollmeyer, T.M. Jahns, R.D. Lorenz, IEEE Transportation Electrification Conference and Expo (ITEC 2014): Dearborn, Michigan, USA, 15 - 18 June 2014, IEEE, Piscataway, NJ, 2014, pp. 1–8, 2014.
[35] H. Ge, T. Aoki, N. Ikeda, S. Suga, T. Isobe, Z. Li, Y. Tabuchi, J. Zhang, J. Electrochem. Soc. 164 (2017) A1050–A1060, https://doi.org/10.1149/2.0461706jes.
[36] M. Petzl, M.A. Danzer, J. Power Sources 254 (2014) 80–87, https://doi.org/10.1016/j.jpowsour.2013.12.060.
[37] M. Ouyang, Z. Chu, L. Lu, J. Li, X. Han, X. Feng, G. Liu, J. Power Sources 286 (2015) 309–320, https://doi.org/10.1016/j.jpowsour.2015.03.178.
[38] M. Bozorgchenani, G. Kucinskis, M. Wohlfahrt-Mehrens, T. Waldmann, J. Electrochem. Soc. 169 (2022), 30509, https://doi.org/10.1149/1945-7111/ac580d.
[39] M. Alipour, C. Ziebert, F.V. Conte, R. Kizilel, Batteries 6 (2020) 35, https://doi.org/10.3390/batteries6030035.
[40] S. Ma, M. Jiang, P. Tao, C. Song, J. Wu, J. Wang, T. Deng, W. Shang, Prog. Nat. Sci.: Mater. Int. 28 (2018) 653–666, https://doi.org/10.1016/j.pnsc.2018.11.002.
[41] L. Su, J. Zhang, J. Huang, H. Ge, Z. Li, F. Xie, B.Y. Liaw, J. Power Sources 315 (2016) 35–46, https://doi.org/10.1016/j.jpowsour.2016.03.043.
[42] M. Schimpe, M.E. von Kuepach, M. Naumann, H.C. Hesse, K. Smith, A. Jossen, J. Electrochem. Soc. 165 (2018) A181–A193, https://doi.org/10.1149/2.1181714jes.
[43] K.L. Gering, S.V. Sazhin, D.K. Jamison, C.J. Michelbacher, B.Y. Liaw, M. Dubarry, M. Cugnet, J. Power Sources 196 (2011) 3395–3403, https://doi.org/10.1016/j.jpowsour.2010.05.058.
[44] M. Dubarry, G. Baure, A. Devie, J. Electrochem. Soc. 165 (2018) A773–A783, https://doi.org/10.1149/2.0421805jes.
[45] T. Raj, A.A. Wang, C.W. Monroe, D.A. Howey, Batteries & Supercaps 3 (2020) 1377–1385, https://doi.org/10.1002/batt.202000160.
[46] E. Coron, S. Geniès, M. Cugnet, P.X. Thivel, J. Electrochem. Soc. 167 (2020), 110556, https://doi.org/10.1149/1945-7111/aba703.
[47] E.V. Thomas, I. Bloom, J.P. Christophersen, V.S. Battaglia, J. Power Sources 184 (2008) 312–317, https://doi.org/10.1016/j.jpowsour.2008.06.017.
[48] M. Bauer, C. Guenther, M. Kasper, M. Petzl, M.A. Danzer, J. Power Sources 283 (2015) 494–504, https://doi.org/10.1016/j.jpowsour.2015.02.130.
[49] E. Coron, S. Geniès, M. Cugnet, P.X. Thivel, J. Electrochem. Soc. 168 (2021), 100539, https://doi.org/10.1149/1945-7111/ac3112.
[50] W. Chang, C. Bommier, T. Fair, J. Yeung, S. Patil, D. Steingart, J. Electrochem. Soc. 167 (2020), 90503, https://doi.org/10.1149/1945-7111/ab6c56.
[51] B. Rumberg, B. Epding, I. Stradtmann, A. Kwade, J. Energy Storage 25 (2019), 100890, https://doi.org/10.1016/j.est.2019.100890.
[52] M. Flügel, K. Richter, M. Wohlfahrt-Mehrens, T. Waldmann, J. Electrochem. Soc. 169 (2022), 50533, https://doi.org/10.1149/1945-7111/ac70af.
[53] K. Richter, T. Waldmann, N. Paul, N. Jobst, R.-G. Scurtu, M. Hofmann, R. Gilles, M. Wohlfahrt-Mehrens, ChemSusChem 13 (2020) 529–538, https://doi.org/10.1002/cssc.201903139.
[54] M. Petzl, M. Kasper, M.A. Danzer, J. Power Sources 275 (2015) 799–807, https://doi.org/10.1016/j.jpowsour.2014.11.065.
[55] P.M. Attia, A. Bills, F. Brosa Planella, P. Dechent, G. dos Reis, M. Dubarry, P. Gasper, R. Gilchrist, S. Greenbank, D. Howey, O. Liu, E. Khoo, Y. Preger, A. Soni, S. Sripad, A.G. Stefanopoulou, V. Sulzer, J. Electrochem. Soc. 169 (2022), 60517, https://doi.org/10.1149/1945-7111/ac6d13.
[56] S. Radloff, L.S. Kremer, A. Hoffmann, M. Wohlfahrt-Mehrens, Mater. Today Commun. 28 (2021), 102549, https://doi.org/10.1016/j.mtcomm.2021.102549.
[57] W. Vermeer, G.R. Chandra Mouli, P. Bauer, IEEE Trans. Transp. Electrific. 8 (2022) 2205–2232, https://doi.org/10.1109/TTE.2021.3138357.
[58] S.K. Rechkemmer, X. Zang, W. Zhang, O. Sawodny, J. Energy Storage 30 (2020), 101547, https://doi.org/10.1016/j.est.2020.101547.
[59] M. Ecker, J.B. Gerschler, J. Vogel, S. Käbitz, F. Hust, P. Dechent, D.U. Sauer, J. Power Sources 215 (2012) 248–257, https://doi.org/10.1016/j.jpowsour.2012.05.012.
[60] J. Stadler, C. Krupp, M. Ecker, J. Bandlow, B. Spier, A. Latz, J. Power Sources 521 (2022), 230952, https://doi.org/10.1016/j.jpowsour.2021.230952.
[61] M. Koseoglou, E. Tsioumas, D. Ferentinou, I. Panagiotidis, N. Jabbour, D. Papagiannis, C. Mademlis, J. Energy Storage 54 (2022), 105345, https://doi.org/10.1016/j.est.2022.105345.
[62] S. Hein, A. Latz, Electrochim. Acta 201 (2016) 354–365, https://doi.org/10.1016/j.electacta.2016.01.220.
[63] A.F.J. Levi, Applied Quantum Mechanics, second ed., Cambridge University Press, Cambridge, 2006.
[64] Y. Abe, S. Kumagai, J. Energy Storage 19 (2018) 96–102, https://doi.org/10.1016/j.est.2018.07.012.
[65] M. Lewerenz, A. Marongiu, A. Warnecke, D.U. Sauer, J. Power Sources 368 (2017) 57–67, https://doi.org/10.1016/j.jpowsour.2017.09.059.
[66] X.-G. Yang, Y. Leng, G. Zhang, S. Ge, C.-Y. Wang, J. Power Sources 360 (2017) 28–40, https://doi.org/10.1016/j.jpowsour.2017.05.110.
[67] M. Wohlfahrt-Mehrens, C. Vogler, J. Garche, J. Power Sources 127 (2004) 58–64, https://doi.org/10.1016/j.jpowsour.2003.09.034.
[68] T. Waldmann, N. Ghanbari, M. Kasper, M. Wohlfahrt-Mehrens, J. Electrochem. Soc. 162 (2015) A1500–A1505, https://doi.org/10.1149/2.0411508jes.
[69] T. Joshi, K. Eom, G. Yushin, T.F. Fuller, J. Electrochem. Soc. 161 (2014) A1915–A1921, https://doi.org/10.1149/2.0861412jes.